

The voltage dependence of  $\tau$  produces a voltage dependence of the current, which is observed by measuring the amplitude of the FMR-like oscillations as a function of  $U_s$  (in Fig. 3b at position C). Again, we consider a high pumping power (filled circles) of  $1.5 \text{ mJ cm}^{-2}$  and a pumping power reduced by a factor of about three (open circles,  $0.5 \text{ mJ cm}^{-2}$ ). In this figure there are two voltage ranges: in one range ( $U_s \leq -0.6 \text{ V}$ )—the reversed bias voltage range in the diode—the amplitude is almost constant, and scales roughly linearly with the pumping power. In this range, the whole system formed by the Schottky barrier and the magnetic film acts in a linear way. In the other range ( $U_s \geq -0.6 \text{ V}$ )—at high pumping power—the amplitude decreases until  $U_s \approx 0.4 \text{ V}$  (we did not apply higher voltages to avoid damaging the diode because of the high d.c. current flow). For low pumping power the amplitude does not show a significant change, and the curves for high and low pumping power begin to approach each other for  $U_s \geq -0.5 \text{ V}$ . Notice that, when  $U_s$  changes sign, the oscillation neither reverses its sign nor vanishes. Evidently, we are dealing with a Schottky junction, where, even at positive voltages, the bands are still bent in the depletion region (see the band scheme in Fig. 3c). At high pumping power, the drop of the oscillation amplitude coincides with the increase of the carrier sweep-out time. With increasing carrier sweep-out time—but at constant number of carriers—the maximum magnetic field strength decreases, and thus the oscillation amplitude should decrease as observed. For low pumping power, only a very weak decrease of the amplitude can be picked up in our experiment, coinciding with a moderate increase of the sweep-out time.

We conclude that this Schottky diode works as a voltage-dependent 'magnetic field pump'. The most straightforward application of this approach to ultrafast production of magnetic fields is in the emerging experimental field of precessional dynamics. Because of the high degree of integration, our device avoids all the usual constructions required when a magnetic field that has been generated in an ultrafast fashion is brought to a magnetic element from a distant source. The field pulse is not distorted by reflections in mismatched electrical waveguides that transport current pulses from the source to a magnetic element, as the pulse is generated within the magnetic element itself. As the maximum induced magnetic field scales with the reciprocal of the spot size, reducing the size of the light spot or using hybrid junctions laterally patterned to nanometre diameters might produce sufficiently strong fields to excite precessional switching. □

Received 23 August; accepted 27 September 2001.

1. Hiebert, W. K., Stankiewicz, A. & Freeman, M. R. Direct observation of magnetic relaxation in a small permalloy disk by time-resolved scanning Kerr microscopy. *Phys. Rev. Lett.* **79**, 1134–1137 (1997).
2. Crawford, T. M., Silva, T. J., Teplin, C. W. & Rogers, C. T. Subnanosecond magnetization dynamics measured by the second-harmonic magneto-optic Kerr effect. *Appl. Phys. Lett.* **74**, 3386–3388 (1999).
3. Hicken, R. J. & Wu, J. Observation of ferromagnetic resonance in the time domain. *J. Appl. Phys.* **85**, 4580–4582 (1999).
4. Acremann, Y. *et al.* Imaging precessional motion of the magnetization vector. *Science* **290**, 492–495 (2000).
5. Bauer, M., Lopusnik, R., Fassbender, J. & Hillebrands, B. Suppression of magnetic-field pulse-induced magnetization precession by pulse tailoring. *Appl. Phys. Lett.* **76**, 2758–2760 (2000).
6. Choi, B. C., Belov, M., Hiebert, W. K., Ballentine, G. E. & Freeman, M. R. Ultrafast magnetization reversal dynamics investigated by time domain imaging. *Phys. Rev. Lett.* **86**, 728–731 (2001).
7. Back, C. H. *et al.* Minimum field strength in precessional magnetization reversal. *Science* **285**, 864–867 (1999).
8. Slonczewski, J. C. Current-driven excitation of magnetic multilayers. *J. Magn. Magn. Mater.* **159**, L1–L7 (1996).
9. Berger, L. Emission of spin waves by a magnetic multilayer traversed by a current. *Phys. Rev. B* **54**, 9353–9358 (1996).
10. Weber, W., Riesen, S. & Siegmann, H. C. Magnetization precession by hot spin injection. *Science* **291**, 1015–1018 (2001).
11. Tsoi, M. *et al.* Excitation of a magnetic multilayer by an electric current. *Phys. Rev. Lett.* **80**, 4281–4284 (1998).
12. Myers, E. B. *et al.* Current-induced switching of domains in magnetic multilayer devices. *Science* **285**, 867–870 (1999).
13. Wegrowe, J.-E. *et al.* Current-induced magnetization reversal in magnetic nanowires. *Europhys. Lett.* **45**, 626–670 (1999).
14. Fiederling, R. *et al.* Injection and detection of a spin-polarized current in a light-emitting diode. *Nature* **402**, 787–789 (1999).
15. Ohno, Y. *et al.* Electrical spin injection in a ferromagnetic semiconductor heterostructure. *Nature* **402**,

- 790–792 (1999).
16. Zhu, J.-G., Zheng, Y. & Prinz, G. A. Ultrahigh density vertical magnetoresistive random access memory. *J. Appl. Phys.* **87**, 6668–6673 (2000).
17. Prinz, G. A., Rado, G. T. & Krebs, J. J. Magnetic properties of single-crystal (110) iron films grown on GaAs by molecular beam epitaxy. *J. Appl. Phys.* **53**, 2087–2091 (1982).
18. Dumm, M. *et al.* Magnetism of ultrathin FeCo (001) films on GaAs(001). *J. Appl. Phys.* **87**, 5457–5459 (2000).
19. Kittel, C. On the theory of ferromagnetic resonance absorption. *Phys. Rev.* **73**, 155–161 (1948).
20. Koopmans, B., Van Kampen, M., Kohlhepp, J. T. & de Jonge, W. J. M. Ultrafast magneto-optics in nickel: magnetism or optics? *Phys. Rev. Lett.* **85**, 844–847 (2000).
21. Ganping, Yu *et al.* Ultrafast time resolved photoinduced magnetization rotation in a ferromagnetic/antiferromagnetic exchange coupled system. *Phys. Rev. Lett.* **82**, 3705–3708 (1999).
22. Christianen, P. C. M. *et al.* Ultrafast carrier dynamics at a metal-semiconductor interface. *J. Appl. Phys.* **80**, 6831–6838 (1996).

**Acknowledgements**

This work was supported by ETH Zurich, the Swiss National Foundation and the Deutsche Forschungsgemeinschaft.

Correspondence and requests for materials should be addressed to D.P. (e-mail: pescia@solid.phys.ethz.ch).

.....

## Imaging the atomic arrangements on the high-temperature reconstructed $\alpha\text{-Al}_2\text{O}_3(0001)$ surface

**Clemens Barth & Michael Reichling**

*Department Chemie, Universität München, Butenandtstraße 5-13 E, 81377 München, Germany*

.....

Alumina is a technologically important oxide crystal because of its use as a catalyst and as a substrate for microelectronic applications<sup>1</sup>. A precise knowledge of its surface atomic structure is a prerequisite for understanding and controlling the physical processes involved in many of its applications<sup>2</sup>. Here we use a dynamic scanning force microscopy technique<sup>3</sup> to image directly the atomic structure of the high-temperature phase of the  $\alpha\text{-Al}_2\text{O}_3(0001)$  surface. Evidence for a surface reconstruction appears as a grid of protrusions that represent a rhombic unit cell, and we confirm that the arrangement of atoms is in the form of surface domains with hexagonal atomic order at the centre and disorder at the periphery. We show that, on exposing the surface to water and hydrogen, this surface structure is important in the formation of hydroxide clusters. These clusters appear as a regular pattern of rings that can be explained by self-organization processes involving cluster–surface and cluster–cluster interactions. Alumina has long been regarded as the definitive test for atomic-resolution force microscopy of insulators so the whole class of insulating oxides should now open for direct atomic-scale surface investigations.

The (0001) surface of  $\alpha\text{-Al}_2\text{O}_3(0001)$  exists in several ordered phases that can reversibly be transformed into each other by thermal treatment and oxygen exposure<sup>4</sup>. The high-temperature phase has long been known to be oxygen-deficient<sup>5</sup>, and electron<sup>6</sup> as well as X-ray diffraction<sup>7</sup> revealed a surface reconstruction with a large  $(\sqrt{31} \times \sqrt{31})R \pm 9^\circ$  unit cell. (Here  $R \pm 9^\circ$  denotes rotation by  $\pm 9^\circ$ ). The details and topography of this atomic structure were, however, never unambiguously revealed. Although a cubic arrangement of surface Al atoms was concluded from early low-energy electron diffraction studies<sup>4</sup>, results from a later, very elaborate, crystallographic study of X-ray diffraction data pointed to a hexagonal symmetry<sup>7</sup> and a model was developed proposing a surface structure composed of hexagonal domains with perfect

hexagonal order in the centre and disorder at the domain boundaries<sup>7,8</sup>. As alumina is a good insulator, an investigation of its surface with scanning tunnelling microscopy is impossible, so scanning force microscopy (SFM) appears to be the only technique capable of directly imaging this surface. So far, however, imaging capabilities were limited to the nanometre scale rather than atomic resolution<sup>9–12</sup>.

Recently, we developed dynamic-mode SFM to yield atomic resolution on fluoride surfaces<sup>13</sup> and here we apply this technique to  $\alpha$ -Al<sub>2</sub>O<sub>3</sub>(0001) with the aim of clarifying the structural details of this surface on the atomic scale. Dynamic-mode SFM primarily measures the frequency detuning of the oscillation of a cantilever that is due to the interaction of the attached sensing tip with the surface<sup>14</sup>. In standard operation, a high gain feedback loop is installed, regulating the tip–surface distance according to the frequency detuning to obtain an image that is related to surface topography. For the measurements reported here, however, the loop gain for the topography feedback was set to a comparably low value in order also to obtain a clear contrast in the frequency detuning signal<sup>15</sup> while at the same time gaining information about surface topography<sup>16</sup>. The  $(\sqrt{31} \times \sqrt{31})R + 9^\circ$  recon-

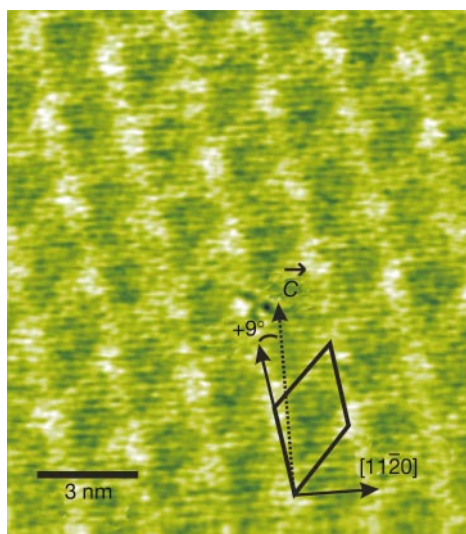


**Figure 1** Structure of the  $\alpha$ -Al<sub>2</sub>O<sub>3</sub>(0001) surface in its  $(\sqrt{31} \times \sqrt{31})R + 9^\circ$  high-temperature reconstruction, as measured by dynamic scanning force microscopy. The reconstruction appears in form of a rhombic grid of protrusions with the highest elevations at the crossing points. The rhombi directly represent the unit cell of the reconstructed surface and are tilted by  $9^\circ$  with respect to the  $c$ -axis of the alumina crystal. Stripes in the  $[11\bar{2}0]$  direction represent rows of aluminium atoms that are the predominant species on this surface. The colour-coded image represents the interaction strength (cantilever oscillation frequency detuning ranging from  $-44.5$  Hz (dark) to  $-48.5$  Hz (bright)) of the force microscope tip with the surface as a function of position. For this and all other measurements, the loop gain of the tip–surface distance control loop was set to a low value to yield weak topographic contrast and maintain a strong detuning signal providing the best contrast for identifying surface structure details. Atomic resolution imaging requires a well prepared tip, minimization of long-range background forces and avoidance of inhomogeneously charged surface areas. The oxidized silicon tip is prepared by repeatedly bringing it into slight contact with the surface and testing the resolution after each try. After preparing a tip yielding atomic resolution, we took great care to preserve the tip atomic structure by avoiding further contact or an excessively close approach to the surface. Atomic contrast is due to chemical interactions between a tip atom and surface ions, and can be separated from the contrast due to background forces<sup>22</sup>. To enhance chemical interaction, the tip–surface distance is manually reduced to the smallest possible values allowing imaging without tip instability. To minimize long-range electrostatic interactions between tip and surface, the bias voltage between the tip and the sample holder is varied and finally fixed at a value yielding minimum frequency detuning<sup>22</sup>.

structed  $\alpha$ -Al<sub>2</sub>O<sub>3</sub>(0001) surface was prepared using standard procedures<sup>17</sup> involving polishing, etching and cycle-heating the crystal to temperatures above  $1,300^\circ\text{C}$  in ultrahigh vacuum.

In Fig. 1 we show the surface structure shortly after preparation. The dominant feature is a rhombic grid representing the unit cell of the  $(\sqrt{31} \times \sqrt{31})R + 9^\circ$  reconstruction. The topography image (not shown here) reveals that the grid is protruding from the crystal. The displacement of atoms out of the surface plane is largest at the edges of the reconstruction rhombi, and contrast from atomic rows in  $[11\bar{2}0]$  direction is best developed in their interiors. More details of the atomic structures can be inferred from the higher-magnification image shown in Fig. 2a that was taken at a reduced tip–surface distance. In this image, the grid structure is only in faint contrast; however, the atomic rows and individual surface atoms can clearly be identified. Image analysis illustrated in Fig. 2b reveals that each side of a rhomb is intersected by ten atomic rows.

This finding is perfectly compatible with the suggested hexagonal atomic structure of the surface<sup>7,8</sup> and excludes the earlier proposed cubic structure that would imply 12 intersecting atomic rows<sup>4</sup>. A hexagonal arrangement of atoms can directly be identified in the interiors of three rhombi but is partly suppressed by a defect in the fourth rhomb. We note, in this and similar images, that such hexagonal arrangements of atoms are well developed almost exclusively in the centre of the rhombi—but these arrangements vanish at their sides and edges. This feature is also well in agreement with the proposed surface structure that predicts order in the centre of hexagonal surface domains and disorder at the domain boundaries<sup>7,8</sup>.

The proposed hexagonal surface domains and the rhombic structure discovered here can be seen to be compatible when both structure models are superimposed as shown in Fig. 3. Ordered regions of rhombi and hexagons coincide while the sides and specifically the edges of the rhombi intersect regions where disorder is expected. Hence, with dynamic scanning force microscopy we could not only directly demonstrate a reconstruction on an insulator that is as large as that of the well known Si(111) $7 \times 7$  surface, but also unambiguously establish hexagonal atomic order on the

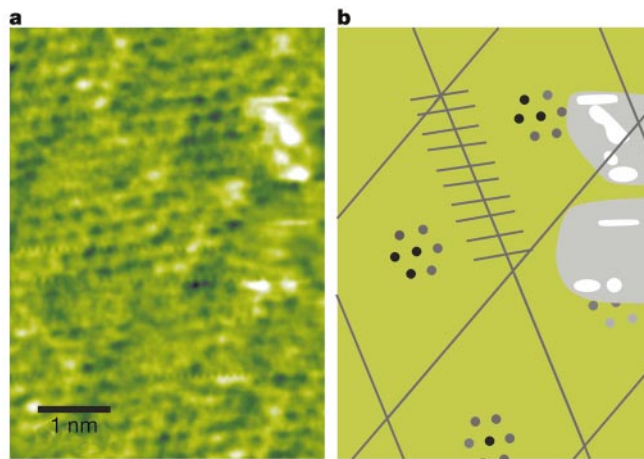


**Figure 2** Section of the surface from Fig. 1 scanned with higher magnification (a) and schematic representation of image features shown on the same scale (b). The magnifying scan was performed at a reduced tip–surface distance that partly suppresses the grid structure but emphasizes the contrast due to individual surface atoms; frequency detuning ranges from  $-53.5$  Hz (dark) to  $-58.5$  Hz (bright). Hexagonal surface order is directly evident from the hexagons most clearly visible in the centres of the reconstruction rhombi but also from the fact that the side of each rhomb is intersected by ten atomic rows (short grey lines in b). This image also reveals disorder in regions far from the rhomb centres. Bright features on the right side are due to surface defects or adsorbates.

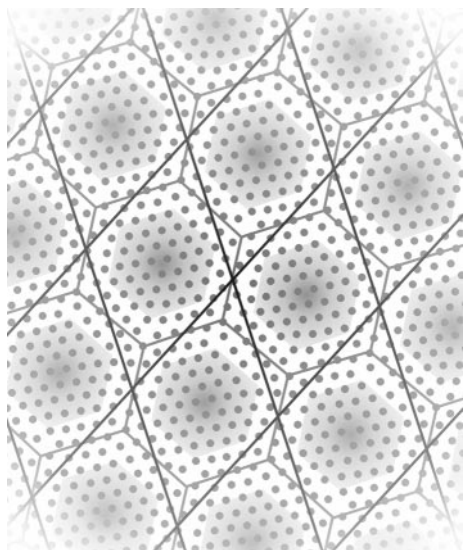


**Figure 3** Schematic representation of the  $(\sqrt{31} \times \sqrt{31})R + 9^\circ$  reconstruction of  $\alpha\text{-Al}_2\text{O}_3(0001)$  with grey dots representing the atoms of the first aluminium layer<sup>8</sup>. The hexagonal pattern reflects onto the domain structure where the aluminium atoms exhibit the nearly perfect hexagonal (111) structure of metallic aluminium<sup>7,8</sup>. The rhombic grid is that found by force microscopy imaging. Bright regions at the periphery of the concentric hexagons and rhombi are those of atomic disorder, while the grey shaded areas in the centre are regions of hexagonal order.

high-temperature reconstructed surface of  $\alpha\text{-Al}_2\text{O}_3(0001)$  and confirm propositions about partial disorder on this surface.

Next, we demonstrate that this rhombic structure may strongly affect adsorption, clustering and crystallization at the surface. After investigating the clean, reconstructed surface, we left it exposed to residual gas that had a pressure of  $4 \times 10^{-8}$  Pa and was predominantly composed of water and hydrogen. Additional scanning force images were taken after dosages of  $5 \times 10^{-4}$  Pa s and  $35 \times 10^{-4}$  Pa s. Even in images (not shown here) taken at the smaller dosage, we observe a significant modification of the surface in form of defects with lateral dimensions ranging from 0.4 nm to 0.8 nm that are preferentially located in the edges of the rhombi. The number of such defects increases with exposure time and after about two days we find an unusual, regular structure of rings composed of up to eight defects, as exhibited in Fig. 4. This figure shows the rings forming a network reproducing the rhomboidal structure of the reconstructed surface. From the preferential development of defects in rhomb corners observed at lower exposures we conclude that the rings are centred at corners. This implies that the defects are preferentially stabilized in regions of disorder and maximum protrusion, which seems plausible since there we would intuitively expect lower coordination and higher chemical activity than in regions with a more regular atomic structure. This ordering into rings indicates a significant interaction between defects.

The size of the defects implies that they are not single molecules but clusters formed from species appearing when the surface is dosed with water. Their chemical composition, however, cannot be determined with the scanning force microscope and remains a subject for speculation at this stage of investigation. We find strong evidence in the literature for dissociative adsorption of water on the non-reconstructed  $\alpha\text{-Al}_2\text{O}_3(0001)$  surface<sup>18</sup> and it has been pointed out that the aluminium-terminated surface is highly reactive<sup>19</sup>. The high-temperature-reconstructed surface that we investigate here is even more aluminium-enriched, so we anticipate that upon exposure to water, the surface rapidly becomes covered with hydroxyl groups. On the other hand, it has been proposed that hydroxyl groups have significant mobility on the

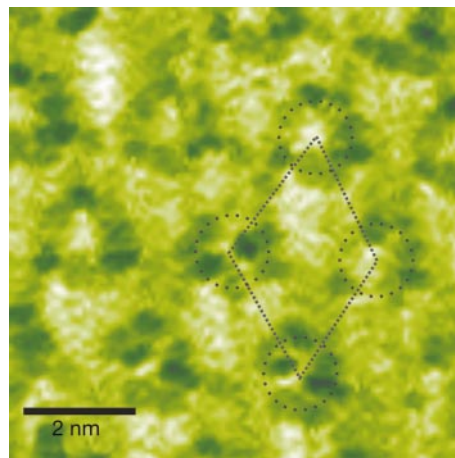


**Figure 4** The reconstructed  $\alpha\text{-Al}_2\text{O}_3(0001)$  surface after exposure to  $35 \times 10^{-4}$  Pa s of water and hydrogen originating from the residual gas of the ultrahigh vacuum. Hydroxide crystallizes into a pattern reproducing the rhomboidal structure of the reconstructed surface. A substructure in form of rings is clearly visible. Rings are centred at the points of highest elevation and largest disorder of the reconstructed surface, and are formed by up to 8 clusters. Each cluster has a size ranging between 0.4 nm and 0.8 nm and is an agglomerate of hydroxide, most probably in the form of crystalline  $\text{Al}(\text{OH})_3$ . In this image, a dark contrast in the frequency detuning (ranging from  $-45$  Hz (dark) to  $-65$  Hz (bright)) corresponds to protrusion in topography. This contrast inversion (compared to Figs 1 and 2) and the much larger detuning range are presumably due to the different chemical interactions between the tip and  $\text{Al}_2\text{O}_3$  and between the tip and the OH clusters. It seems that the distance dependence of tip–surface interaction differs considerably between materials, resulting in a strong chemical contrast when crossing from one material to the other.

surface<sup>20</sup> and can thus condense into clusters at energetically favourable sites. As the shape of individual clusters found in our measurements is surprisingly sharp and regular, we propose that they represent small crystallites of  $\text{Al}(\text{OH})_3$ . In fact, there is experimental evidence for the formation of this species on alumina surfaces under high-pressure conditions<sup>21</sup> and when the surface is hydrated (by rinsing with water)<sup>19</sup>. The extremely high reactivity expected in regions of atomic disorder on our surface readily explains the observed stabilization of  $\text{Al}(\text{OH})_3$  clusters in these regions even under low-pressure conditions.

The ring structure, however, is determined by cluster–cluster interactions and presumably also steric constraints for their arrangement. Thus strong cluster–surface and cluster–cluster interactions create both an overall structure that corresponds to the surface reconstruction and a substructure in the form of clusters grouped in rings that has no evident relation to surface symmetry. These findings for high-temperature-reconstructed, water-exposed  $\alpha\text{-Al}_2\text{O}_3(0001)$  reveal the unusual ability of this surface to structure molecular clusters formed by self-organization of the randomly positioned molecules. □

Received 18 July; accepted 13 September 2001.

1. Henrich, V. E. & Cox, P. A. *The Surface Science of Metal Oxides* (Cambridge Univ. Press, Cambridge, 1994).
2. Campbell, C. T. Ultrathin metal films and particles on oxide surfaces: Structural, electronic and chemisorptive properties. *Surf. Sci. Rep.* **27**(1–3), 1–111 (1997).
3. de Lozanne, A. Atomic force microscopy: You may squeeze the atoms but don't mangle the surface! *Science* **291**, 2561–2562 (2001).
4. French, T. M. & Somorjai, G. A. Composition and surface structure of the (0001) face of  $\alpha$ -alumina by low-energy electron diffraction. *J. Phys. Chem.* **74**, 2489–2495 (1970).
5. Gautier, M., Duraud, J. P., Pham Van, L. & Guittet, M. J. Modifications of  $\alpha\text{-Al}_2\text{O}_3(0001)$  surfaces induced by thermal treatments or ion bombardment. *Surf. Sci.* **250**, 71–80 (1991).
6. Chang, C. C. LEED studies of the (0001) face of  $\alpha$ -alumina. *J. Appl. Phys.* **39**, 5570–5573 (1968).
7. Renaud, G., Villette, B., Vilfan, L. & Bourret, A. Atomic structure of the  $\alpha\text{-Al}_2\text{O}_3(0001)$  ( $\sqrt{31} \times \sqrt{31}R \pm 9^\circ$ ) reconstruction. *Phys. Rev. Lett.* **73**, 1825–1828 (1994).
8. Vilfan, L., Lançon, F. & Villain, J. Rotational reconstruction of sapphire (0001). *Surf. Sci.* **392**, 62–68 (1997).

9. Beitel, G., Markert, K., Wiechers, J., Hrbek, J. & Behm, R. J. in *Adsorption on Ordered Surface of Ionic Solids and Thin Films* (eds Umbach, E. & Freund, H.-J.) 71–82 (Springer, Berlin, Heidelberg, 1993).
10. Pham Van, L., Kurmosikov, O. & Cousty, J. Evolution of steps on vicinal (0001) surfaces of  $\alpha$ -alumina. *Surf. Sci.* **411**, 263–271 (1998).
11. Pang, C. L., Raza, H., Haycock, S. A. & Thornton, G. Growth of copper and palladium on  $\alpha$ -Al<sub>2</sub>O<sub>3</sub>(0001). *Surf. Sci.* **460**, L510–L514 (2000).
12. Sasahara, A., Utesuka, H. & Onishi, H. Noncontact-mode atomic force microscopy of  $\alpha$ -Al<sub>2</sub>O<sub>3</sub>(0001) surface. *Jpn J. Appl. Phys.* **39**, 3773–3776 (2000).
13. Reichling, M. & Barth, C. Scanning force imaging of atomic size defects on the CaF<sub>2</sub>(111) surface. *Phys. Rev. Lett.* **83**(4), 768–771 (1999).
14. Albrecht, T. R., Grütter, P., Horne, D. & Rugar, D. Frequency modulation detection using high-Q cantilevers for enhanced force microscope sensitivity. *J. Appl. Phys.* **69**, 668–673 (1991).
15. Foster, A. S., Barth, C., Shluger, A. L. & Reichling, M. Unambiguous interpretation of atomically resolved force microscopy images of an insulator. *Phys. Rev. Lett.* **86**, 2373–2376 (2001).
16. Barth, C. & Reichling, M. Resolving ions and vacancies at step edges on insulating surfaces. *Surf. Sci. Lett.* **470**, L99–L103 (2000).
17. Toofan, J. & Watson, P. R. The termination of the  $\alpha$ -Al<sub>2</sub>O<sub>3</sub>(0001) surface: a LEED crystallography determination. *Surf. Sci.* **401**, 162–172 (1998).
18. Coustet, V. & Jupille, J. Hydroxyl groups on oxide surfaces. *Il Nuovo Cimento* **19**, 1657–1664 (1997).
19. Eng, P. J. *et al.* Structure of the hydrated  $\alpha$ -Al<sub>2</sub>O<sub>3</sub>(0001) surface. *Science* **288**, 1029–1033 (2000).
20. Hass, K. C., Schneider, W. F., Curioni, A. & Andreoni, W. The chemistry of water on alumina surfaces: reaction dynamics from first principles. *Science* **282**, 265–268 (1998).
21. Liu, P., Kendelewicz, T., Brown, G. E. Jr, Nelson, E. J. & Chambers, S. A. Reaction of water vapor with  $\alpha$ -Al<sub>2</sub>O<sub>3</sub>(0001) and  $\alpha$ -Fe<sub>2</sub>O<sub>3</sub>(0001) surfaces: synchrotron X-ray photoemission studies and thermodynamic calculations. *Surf. Sci.* **417**, 53–65 (1998).
22. Guggisberg, M. *et al.* Separation of interactions by noncontact force microscopy. *Phys. Rev. B* **61**, 11151–11155 (2000).

**Acknowledgements**

We are grateful to A. Foster, H. Knözinger, M. Mozaffari-Afshar, Th. Risse, A. L. Shluger, M. Stoneham, I. Vilfan and K. Yasuda for discussions. The alumina sample was provided by the Fritz-Haber-Institut Berlin and technical support from this side for sample preparation is gratefully acknowledged.

Correspondence and requests for materials should be addressed to M.R. (e-mail: reichling@cup.uni-muenchen.de).

**Photoselective adaptive femtosecond quantum control in the liquid phase**

T. Brixner, N. H. Damrauer, P. Niklaus & G. Gerber

Physikalisches Institut, Universität Würzburg, Am Hubland, 97074 Würzburg, Germany

Coherent light sources can be used to manipulate the outcome of light–matter interactions by exploiting interference phenomena in the time and frequency domain. A powerful tool in this emerging field of ‘quantum control’<sup>1–6</sup> is the adaptive shaping of femtosecond laser pulses<sup>7–10</sup>, resulting, for instance, in selective molecular excitation. The basis of this method is that the quantum system under investigation itself guides an automated search, via iteration loops, for coherent light fields best suited for achieving a control task designed by the experimenter<sup>11</sup>. The method is therefore ideal for the control of complex experiments<sup>7,12–20</sup>. To date, all demonstrations of this technique on molecular systems have focused on controlling the outcome of photo-induced reactions in identical molecules, and little attention has been paid to selectively controlling mixtures of different molecules. Here we report simultaneous but selective multi-photon excitation of two distinct electronically and structurally complex dye molecules in solution. Despite the failure of single parameter variations (wavelength, intensity, or linear chirp control), adaptive femtosecond pulse shaping can reveal complex laser fields to achieve chemically selective molecular excitation. Furthermore, our results prove that phase coherences of the solute molecule persist for more than 100 fs in the solvent environment.

The experimental set-up is shown schematically in Fig. 1. We investigated the use of single-parameter quantum control schemes (variation of wavelength, intensity, and linear chirp) and many-parameter ‘adaptive’ control. The latter methodology uses a femtosecond pulse shaper<sup>8,10,21</sup> capable of producing complex shapes by spectral phase modulation. An automated ‘learning loop’<sup>8</sup> is then iterated, in which an experimental feedback signal from the physical control subject itself guides the algorithm to find laser fields (within a 128-parameter search space) optimized for the control task designed by the experimenter. Cycling through this loop does not require any mechanistic information about the induced photo-processes, and optimum results are found under the given experimental conditions. In our experiments, laser pulses modified in single- or multi-parameter schemes irradiate methanol solutions of DCM (4-dicyanomethylene-2-methyl-6-*p*-dimethylaminostyryl-4H-pyran) and [Ru(dpb)<sub>3</sub>](PF<sub>6</sub>)<sub>2</sub> (where dpb is 4,4’-diphenyl-2,2’-bipyridine). The linear absorption spectra (Fig. 2a) show that electronic excitation requires the absorption of at least two photons at 800 nm. Following excited-state dynamics, emissive charge-separated states are reached in both molecules<sup>22–24</sup>. As these target states spontaneously decay back to the ground state after the interaction with the femtosecond laser pulse is over, their relative emission yields can be used as a measure of the excited-state populations that have been generated by the excitation pulse. The following series of experiments were designed to find out if, and how, coherent light fields could be used to excite selectively one specific molecule (but not another one) within liquid-phase solute/

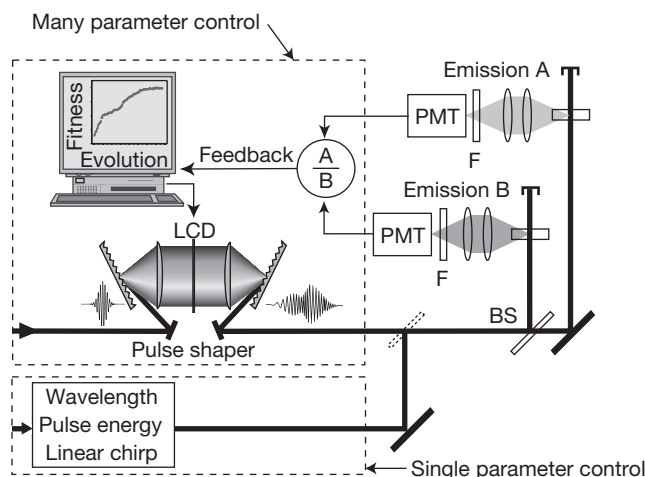


**Figure 1** Experimental set-up. Our femtosecond laser system delivers 80-fs, 1-mJ pulses at a centre wavelength of 800 nm and a repetition rate of 1 kHz. Regarding single-parameter control schemes, the laser power can be varied by attenuation with neutral-density filters, and a spectral transmission window or variable linear chirp can be introduced with a femtosecond pulse shaper<sup>8,10</sup>. This pulse shaper is also used in the many-parameter control scheme to generate complex electric fields. The laser spectrum is dispersed onto a liquid-crystal display (LCD). By applying suitable voltages to 128 independent LCD pixels, optical path lengths can be adjusted for the spatially separated wavelength components, leading to a modulated temporal intensity and phase profile while the spectral intensity distribution remains unchanged. The modified laser pulses are then separated by a beam splitter (BS) and passed unfocused into two flow cells (2 mm length), each containing solutions of different molecular species—shown here as A and B. The emission signals are collected at approximate right angles, spectrally filtered (F) at 650 nm for DCM (A) and at 630 nm for [Ru(dpb)<sub>3</sub>]<sup>2+</sup> (B), detected by photomultiplier tubes (PMT), and temporally integrated by boxcar averagers. The emission ratio of molecule A versus molecule B is used as a feedback signal in a learning loop. We use an evolutionary algorithm as described previously<sup>8</sup>, which (after random initialization) iteratively improves the applied pulse shape until an optimum is found. A population pool of 60 individuals per generation is used, out of which 10 survivors reproduce by cloning (giving rise to 10 children) as well as mutation (10 children) and random pixel crossover between randomly selected parental pairs (40 children).